Excited-state absorption of Cr^{3+} in $LiCaAlF_6$: Effects of asymmetric distortions and intensity selection rules

H. W. H. Lee, Stephen A. Payne, and L. L. Chase
Lawrence Livermore National Laboratory (L-490), University of California, P.O. Box 5508, Livermore, California 94550
(Received 28 November 1988)

We have measured the π-polarized excited-state absorption (ESA) spectra of the new laser material, $LiCaAlF_6:Cr^{3+}$ (hereafter, Cr^{3+}:LiCAF). We have found that the peak cross section of the ESA band is 0.17×10^{-20} cm^2. We are therefore able to explain the high efficiency previously observed for the Cr^{3+}:LiCAF laser by noting that the peak emission cross section of 1.3×10^{-20} cm^2 is much larger than this ESA cross section. As a result, the ESA does not diminish the value of the effective stimulated-emission cross section, in spite of its tendency to overlap the emission band in most Cr^{3+}-doped crystals. It is then shown that the ESA transition is weak relative to the emission band because the t_{2u} distortion present at the Al^{3+} site where the Cr^{3+} substitutes adds transition strength to the π-polarized $^4A_2$-$^4T_2$ absorption and emission features, while it does not contribute oscillator strength to the ESA band. The $^4T_2\rightarrow{}^4T_1a$ ESA band is found to peak near 10030 cm^{-1}, rather than near 7600 cm^{-1} as expected on the basis of simple crystal-field theory. This is explained as being due to the influence of non-totally-symmetric distortions in the excited states of Cr^{3+}.

I. INTRODUCTION

The absorption spectra originating from excited states of ions in crystals are of both basic and practical importance. Excited-state absorption (ESA) can provide information regarding electronic and vibrational properties that cannot be obtained from ordinary absorption or emission measurements. In terms of practical importance, ESA is an important loss mechanism in lasers. Recent work on the ESA of the isoelectronic Cr^{3+} and V^{2+} ions illustrates both of these aspects.[1-4] For those ions which have a $3d^3$ configuration, the fundamentally new information provided by ESA relates to the nature and magnitude of the displacements of the neighboring ions when the excited state is occupied. In particular, it was shown that, contrary to the usual assumptions, non-totally-symmetric (NTS) displacements of the neighbors (such as Jahn-Teller distortions) are of equal or greater importance than the symmetric displacements when orbitally degenerate, or nearly degenerate, excited states are involved.[2] It has also been shown that ESA affects the lasing threshold and slope efficiency of all known tunable Cr^{3+} and V^{2+} lasers.[2,3]

We shall be concerned in this paper with ESA between the $^4T_2$ and ^4T_1a states of the $3d^3$ configuration of Cr^{3+}. Andrews *et al.* first measured this ESA spectrum of Cr^{3+} in $Gd_3Sc_2Ga_3O_{12}$, and suggested that NTS relaxation in the excited state strongly influences the shape of the spectral bands.[1] Soon afterward, Payne, Chase, and Wilke measured the $^4T_2\rightarrow{}^4T_1a$ ESA spectrum of $KMgF_3:V^{2+}$ and developed a plausible explanation of the ESA bands in which it was shown that both the $^4T_2$ and ^4T_1a states were Jahn-Teller (JT) distorted, albeit in opposite senses.[2] The main spectral evidence for the Jahn-Teller effect (JTE) is that the $^4T_2\rightarrow{}^4T_1a$ transition is observed as a broad band rather than as a sharp line, as it is predicted to appear on the basis of simple crystal-field theory, in the absence of the JTE. A simultaneous publication by Moncorge and co-workers[4] confirmed our ESA measurements of V^{2+}.

The spectral observations of the $^4T_2\rightarrow{}^4T_1a$ ESA band show that this ESA feature is likely to spectrally overlap the emission band of Cr^{3+} vibronic laser materials. In a definitive study, Caird *et al.* showed that ESA severely limits the output efficiency of the $Na_3Ga_2Li_3F_{12}:Cr^{3+}$ laser.[3] The low efficiency is due to the reduction in the effective stimulated emission cross section by the ESA band:

$$\sigma_{\text{eff}}=\sigma_{\text{em}}-\sigma_{\text{ESA}}\ , \tag{1}$$

where σ_{em} and σ_{ESA} are the emission and ESA cross sections, respectively.

Interestingly, we have recently shown that $LiCaAlF_6:Cr^{3+}$ (hereafter, Cr^{3+}:LiCAF) lases much more efficiently than $Na_3Ga_2Li_3F_{12}:Cr^{3+}$, and, in agreement, we report in Sec. IV that the peak cross section of the ESA band is much weaker relative to that of the emission band for Cr^{3+}:LiCAF,[5] $\sigma_{\text{ESA}}\ll\sigma_{\text{em}}$. We are able to explain this observation by noting that the odd-parity static fields at the Al site of LiCAF do not add oscillator strength to the ESA transition for reasons of symmetry, while they do increase the cross section of the emission band. In addition, the relaxation energy is found to be smaller in Cr^{3+}:LiCAF compared to $Na_3Ga_2Li_3F_{12}:Cr^{3+}$, thereby leading to reduced spectral overlap of the emission and ESA bands.

This paper is arranged as follows. In Sec. II we outline the experimental details. In Sec. III we report the polarized ground-state absorption spectra of Cr^{3+}:LiCAF, and, on the basis of these spectra and the standard Tanabe-Sugano diagram, predict the peak position of the ESA bands in the absence of the JTE. Perhaps more im-

portantly, we use these ground-state absorption spectra to validate our theory of the intensity-enabling mechanism that is operative for the d-d bands of Cr^{3+}:LiCAF. We then use this theory to explain why the infrared ESA band of Sec. IV is observed to have a relatively low peak cross section. Finally, Sec. V contains a recounting of our conclusions.

II. EXPERIMENTAL

The experimental methods used will be only briefly outlined here. The absorption spectra were recorded with a computer-controlled Cary 17 Spectrophotometer, for which the sample temperature was varied from 20 K to room temperature with a closed-cycle helium refrigeration system.

The excited-state absorption spectrometer has been described in several previous publications,[2,3,6] so we mention only the salient aspects here. The arrangement was essentially of the pump-probe design, in which the pump source was a flashlamp-pumped dye laser, and a cw tungsten-halogen lamp served as the probe. The infrared wavelengths were detected with an InAs diode operated in the photovoltaic mode, while a photomultiplier tube (PMT) was utilized at the visible wavelengths. The spectra obtained with the two detectors were calibrated relative to each other by scanning a short range in both of the spectral regions. The detector output was measured with a boxcar integrator, whose output was then digitized by a computer.

The difference spectra $A_d(\lambda)$ require that the power of the probe beam be measured in the presence (I_p) and the absence (I_u) of the pump pulse,

$$A_d = -\ln(I_p/I_u) \ . \tag{2}$$

It is apparent from Eq. (2) that the ESA bands will be observed as positive features, while ground-state bleaching will give rise to negative signals.

In practice, the actual signals involved probe intensity changes that were sometimes on the order of 0.1%. Therefore, the effects of electronic noise and any fluorescence background must be accurately taken into account to determine the value of A_d. To do this, a cycle consisting of four measurements is required. For small changes in the probe intensity, the following algorithm may be used:

$$A_d = \frac{[I(\text{probe only}) - I(\text{neither})] - [I(\text{pump+probe}) - I(\text{probe only})]}{[I(\text{probe only}) - I(\text{neither})]} \ . \tag{3}$$

A computer served as the clock and generated the pulses needed to appropriately trigger the laser and boxcar integrator, operate a shutter to block the probe beam, and step the monochromator, so as to acquire measurements of all the quantities indicated in Eq. (3). The low-temperature ESA spectra were obtained by using a liquid-nitrogen conductor dewar to cool the sample.

The Cr^{3+}:$LiCaAlF_6$ single crystal was grown by Newkirk of Lawrence Livermore National Laboratory; for the details of crystal growth see Ref. 5.

III. GROUND-STATE ABSORPTION SPECTRA

The Cr^{3+} impurity in $LiCaAlF_6$ (LiCAF) is expected to substitute for the Al^{3+} cation, and, as a result, be surrounded by six fluorines in a nearly octahedral arrangement. The LiCAF host is uniaxial, and, for completeness, the absorption spectra must be acquired with the electric vector of the light field polarized both parallel (π) and perpendicular (σ) to the c axis of the crystal. These absorption data appear in Figs. 1 and 2. The absorption features will be explained in two sections. In Sec. III A the Tanabe-Sugano diagram will be utilized to assign the transitions as they are labeled in the lowest frames of Figs. 1 and 2. Then, in Sec. III B the crystal structure of LiCAF is considered in detail, and it is shown that the static odd-parity distortion at the Al^{3+} site is responsible for the polarization dependence of the absorption bands.

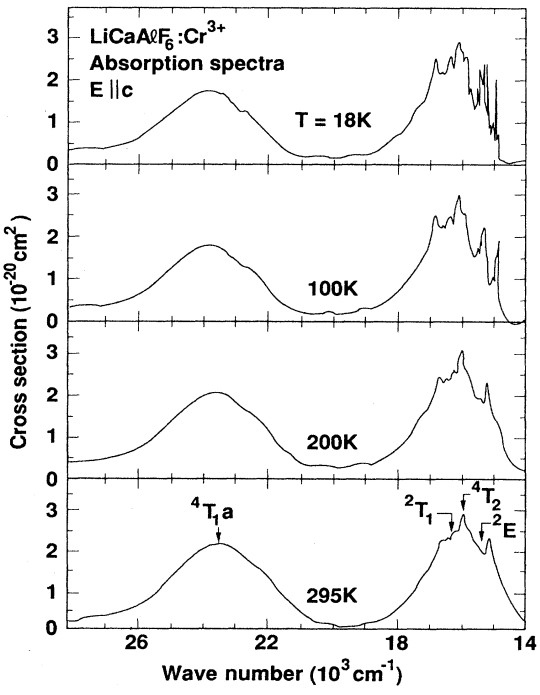

FIG. 1. E||c polarized absorption spectra of $LiCaAlF_6$:Cr^{3+} at the indicated temperatures. The sample was 8.5 mm long and contained 0.29×10^{20} Cr-ions/cm^3. The energetic positions of the final states are denoted in the lowest frame.

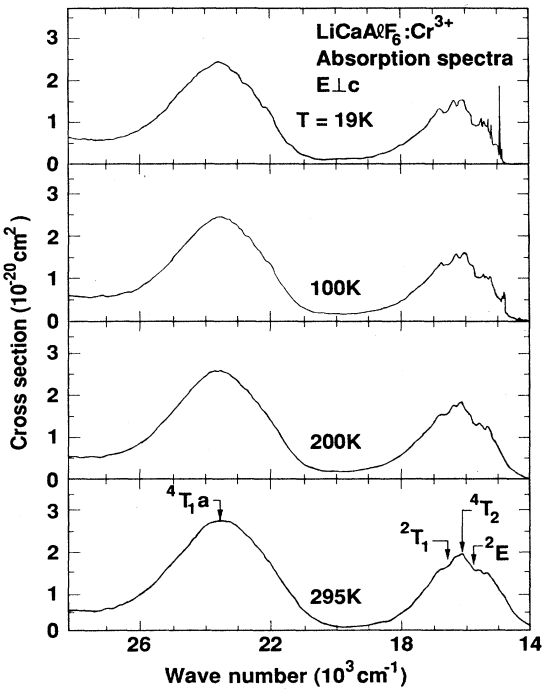

FIG. 2. E⊥c polarized absorption spectra of $LiCaAlF_6$:Cr^{3+} at the indicated temperatures. The sample was 8.5 mm long and contained 0.29×10^{20} Cr-ions/cm^3. The energetic positions of the final states are denoted in the lowest frame.

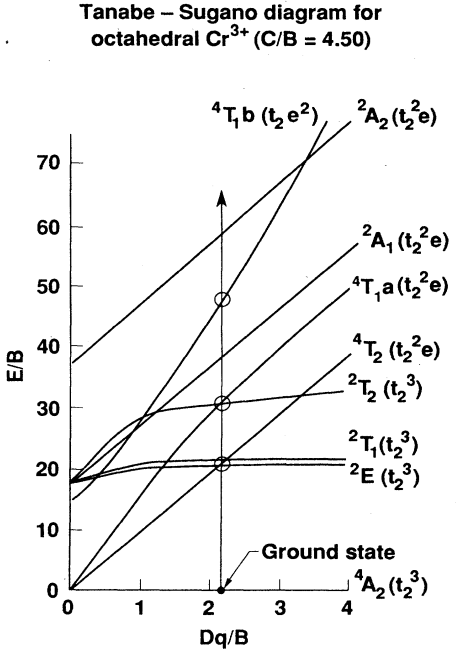

FIG. 3. Tanabe-Sugano diagram for octahedrally coordinated Cr^{3+}. The values of $Dq=1590$ cm^{-1} and $B=745$ cm^{-1} were derived from the absorption peaks at room temperature shown in Figs. 1 and 2. The vertical line at $Dq/B=2.15$ presents the best fit.

A. Energy-level assignments

The energy levels of Cr^{3+} in octahedral environments are generally understood by referring to the standard Tanabe-Sugano diagram, which is reproduced in Fig. 3.[7,8] The abscissa is the ratio of the crystal-field splitting parameter Dq to the electron-electron repulsion integral B. Conventionally, the spectra of Cr^{3+} are fitted with values of Dq and B; for the case of Cr^{3+}:LiCAF, we can use the assignments shown in the lowest frames of Figs. 1 and 2 to find that $B=740$ cm^{-1} and $Dq=1590$ cm^{-1}. The vertical line in Fig. 3 indicates the energy levels obtained for $Dq/B=2.15$.

The broad bands seen in Figs. 1 and 2 are the $^4A_2\rightarrow{}^4T_2$ and $^4A_2\rightarrow{}^4T_1a$ transitions, while the sharp features arise from the $^4A_2\rightarrow{}^2E$ and $^2T_1$ transitions. The widths of the absorption features are most simply explained using the "strong-field" approach.[9] Here, it is recognized that the degeneracy of the $3d$ orbitals is lifted and they are split into two e_g and three t_{2g} components, with the t_{2g} orbitals lying lower. Now, since the $^4A_2$ ground state, as well as the ^2E, $^2T_1$, and $^2T_2$ states, have the t_2^3 strong-field electron configuration, all of these states are expected to have a similar equilibrium configuration in the crystal lattice; the $^4A_2\rightarrow{}^2E$ and $^4A_2\rightarrow{}^2T_1$ transitions are therefore observed as narrow lines. On the other hand, the $^4A_2\rightarrow{}^4T_2$ and ^4T_1a transitions involve the $t_2^3\rightarrow t_2^2e$ electronic configuration change, and the different equilibrium configurations between the states result in the broadband spectra. Based on this understanding, we can simplistically argue that the $^4T_2(t_2^2e)\rightarrow{}^4T_1(t_2^2e)$ excited-state absorption (ESA) transition should be observed as a narrow line near 7600 cm^{-1}; in Sec. IV we show that this ESA band is, in fact, observed as a broad band, due to the influence of the Jahn-Teller effect.

B. Intensity-enabling mechanisms

The absorption bands depicted in Figs. 1 and 2 arise from $3d\rightarrow3d$ type transitions, and for the hypothetical case of the Cr^{3+} ion being in spherical symmetry, the oscillator strength would be zero. The introduction of the ion into a crystal host, however, results in the mixing of the free-ion wave functions such that oscillator strength is induced into the $3d\rightarrow3d$ transitions. In particular, it is required that the symmetry associated with the center of inversion be destroyed by the neighboring ions in the crystal host. This may be accomplished both dynamically (via odd-parity vibrations) and statistically (as a result of the odd-parity distortions present in the crystal structure at the Al^{3+} site). The $^4A_2\rightarrow{}^4T_1a$ transition is observed to increase in intensity by about 40% in passing from 18 K to room temperature; a similar increase occurs for the $^4A_2\rightarrow{}^4T_2$ band. These increases are proof of the existence of the dynamically induced intensity mechanism,[10] since, at higher temperature, more of the odd-parity vibrations become populated, and the average odd-parity distortion is increased.

From Figs. 1 and 2 it is apparent that at 18 K (where the dynamical effects are minimized), the E||c (π) and

$E \perp c$ (σ) polarized spectra differ quite substantially; the ${}^4A_2 \rightarrow {}^4T_2$ band is about 80% stronger in the π spectrum, while the ${}^4A_2 \rightarrow {}^4T_1 a$ transition is enhanced by 40% in the σ polarization. This polarization dependence can only be explained by carefully examining the crystal structure of LiCAF. At this point, we digress to determine the nature of the static crystalline field that is present at the Al^{3+} site.

The crystal structure of $LiCaAlF_6$ is shown in Fig. 4. This figure was reproduced from the work of Viebahn.[11] The unit cell of the LiCAF structure is displayed in the upper frame. It is clear that all the metal cations are surrounded by six fluorines. Inspection of the figure also reveals that the Li and Al ions alternate with the Ca ions in filling the octahedral holes existing between successive layers of fluorines. As a consequence, the Al sites are substantially separated from one another and do not share fluorine neighbors.

We now focus our attention on the Al^{3+} site, since Cr^{3+} substitutionally replaces this ion. Figure 4(b) depicts the percentage of the c-axis unit-cell dimension at which the metal and fluorine ions are located. The Al ion is at 25% of the c-axis dimension, and it is seen that there are three fluorines at 14% and three at 36%. Thus, the c axis corresponds to the trigonal axis of the AlF_6 octahedron. If the Al were situated in a perfect octahedron of fluorines, all the Al-F distances would be equal, and the F—Al—F bond angles would be either 90° or 180°. While the Al-F separations are all 1.80 Å, the bond angles differ slightly from the perfect octahedron requirements.

The distortions present at the Al site can be understood by performing two symmetry-lowering operations upon a hypothetical perfect AlF_6 octahedron. In what follows, we identify the symmetries of these distortions by their representation in the O_h group of the undistorted octahedron. First, the planes of three fluorines located above and below the Al ion must be moved slightly closer together [see Fig. 4(b)]. As a result of this operation the F(1)—Al—F(3) bond angle changes from 90° to 90.87°. This distortion is of even parity (t_{2g} type), and may introduce a small trigonal field splitting in the ${}^4T$ states.

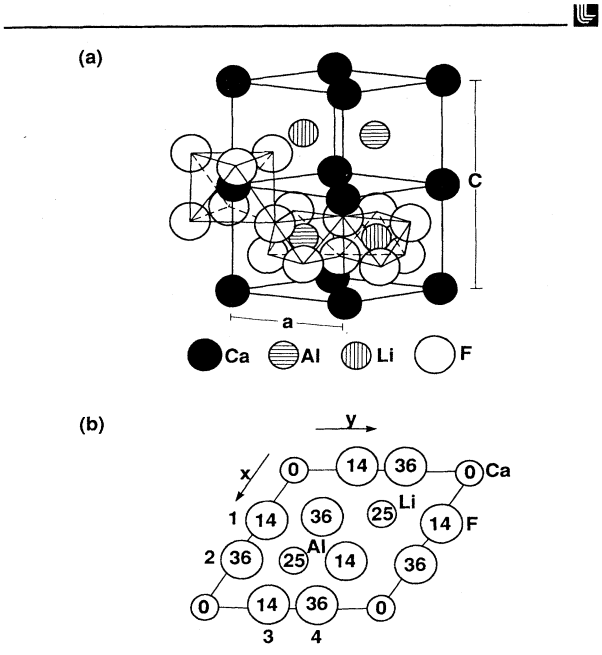

FIG. 4. Unit cell of the $LiCaAlF_6$ crystal, as reproduced from Viebahn (Ref. 11). The numbers in the circles in (b) are the percent height of the ions relative to the full c-axis dimension of the unit cell.

The second symmetry-lowering operation involves the destruction of the center of inversion, and therefore will induce oscillator strength into the d-d transitions. We may imagine that the upper equilateral triangle of fluorines is rotated slightly clockwise (as viewed from above), and that the lower three fluorines are rotated counterclockwise. The result is that the F(1)—Al—F(2) angle is decreased to 87.15°, and the F(2)—Al—F(3) angle is increased to 91.17° [see Fig. 4(b)]. This symmetry operation can be described by the t_{2u} representation, according to the theory of groups. We now show that this t_{2u} distortion is responsible for the polarization dependence of the absorption bands displayed in Figs. 1 and 2.

In general, the transition rate from state $|G\rangle$ to $|F\rangle$ can be described with Fermi's golden rule,[12]

$$R = \frac{2\pi}{\hbar^2} |\langle G|\boldsymbol{\mu}\cdot\mathbf{E}|F\rangle|^2 , \tag{4}$$

where $\boldsymbol{\mu}$ describes the dipole interaction with the light field $\mathbf{E}$. Since the d-d transitions are nominally forbidden, the static t_{2u} distortion described above will induce oscillator strength into the d-d transitions by mixing states $|I\rangle$ into the ground and final states. The condition for this to occur is

$$\sum_I \left[\frac{\langle G|V_u|I\rangle\langle I|\boldsymbol{\mu}|F\rangle}{E_I - E_G} + \frac{\langle G|\boldsymbol{\mu}|I\rangle\langle I|V_u|F\rangle}{E_I - E_F} \right] \neq 0 , \tag{5}$$

where V_u is the *ungerade* electrostatic potential of the static distortion and the E are the energies of the indicated states. Utilizing closure, the transition rate induced by the V_u distortion is, to within a constant,

$$R_\alpha = |\langle G|V_u \mu_\alpha|F\rangle|^2 , \tag{6}$$

where $\alpha = \pi$ or σ describes the state of polarization. On the basis of group theory, and the crystal structure of LiCAF, we can describe the symmetry properties of V_u with[13]

$$V_u \rightarrow \frac{1}{\sqrt{3}}(t_{2u}\xi + t_{2u}\eta + t_{2u}\zeta) , \tag{7}$$

where the Al—F bonds are the x, y, and z axes, to which these basis functions are referred. The symmetries of the π- and σ-polarized light fields can be described with

$$\mu_\pi \rightarrow \frac{1}{\sqrt{3}}(t_{1u}x + t_{1u}y + t_{1u}z) , \tag{8a}$$

$$\mu_\sigma \rightarrow \frac{1}{\sqrt{2}}(t_{1u}x - t_{1u}y) . \tag{8b}$$

TABLE I. Calculation of the Cr^{3+} transition strengths resulting from the static t_{2u} crystal-field distortion of LiCAF (all representations are gerade).

Transition	Transition strength R_α E‖c (π)	E⊥c (σ)
$^4A_2(t_2^3)\rightarrow{}^4T_2(t_2^2e)$	$\frac{2}{3}\lvert\langle t_2\rVert t_1\rVert e\rangle\rvert^2$	$\frac{1}{6}\lvert\langle t_2\rVert t_1\rVert e\rangle\rvert^2$
$^4A_2(t_2^3)\rightarrow{}^4T_1a(t_2^2e)$	0	$\frac{1}{2}\lvert\langle t_2\rVert t_2\rVert e\rangle\rvert^2$
$^4T_2(t_2^2e)\rightarrow{}^4T_1(t_2^2e)$		
Band 1	$\frac{1}{6}\lvert\langle t_2\rVert t_1\rVert t_2\rangle\rvert^2$	$\frac{1}{24}\lvert\langle t_2\rVert t_1\rVert t_2\rangle\rvert^2$ $+\frac{1}{8}\lvert\langle t_2\rVert t_2\rVert t_2\rangle\rvert^2$
Band 2	$\frac{1}{3}\lvert\langle e\rVert a_2\rVert e\rangle\rvert^2$ (=0 for d orbitals)	0

Using the tables of Griffith[14] we couple Eq. (8) with (7), as required by Eq. (6), to obtain

$$V_u\mu_\pi\rightarrow\frac{1}{\sqrt{3}}a_{2g}\alpha-\frac{\sqrt{2}}{3}(t_{1g}x+t_{1g}y+t_{1g}z) \tag{9a}$$

and

$$V_u\mu_\sigma\rightarrow\frac{-1}{\sqrt{3}}e_g\theta+\frac{1}{2\sqrt{3}}(t_{1g}x-t_{1g}y) -\frac{1}{2\sqrt{3}}(2t_{2g}\xi-t_{2g}\xi-t_{2g}\eta)\ . \tag{9b}$$

The three states of interest here are the $^4A_2(t_2^3)$, $^4T_2(t_2^2e)$, and $^4T_1(t_2^2e)$ states. According to the strong-field orbital descriptions, we can decompose each of the states, $|D\Delta\rangle$, as [8]

$$|D\Delta\rangle=\sum_{\alpha,\beta,\gamma}X^{\Delta}_{\alpha\beta\gamma}|a\alpha\rangle|b\beta\rangle|c\gamma\rangle\ , \tag{10}$$

where $|a\alpha\rangle$, $|b\beta\rangle$, and $|c\gamma\rangle$ represent the components of the e_g and t_{2g} orbitals. By substituting Eqs. (9) and (10) into (6), we calculate the oscillator strengths that are induced into the transitions of interest, up to the value of a reduced matrix element. The results of these calculations appear in Table I.

From Table I we see that the accounting of the static t_{2u} field of LiCAF successfully explains the polarization dependence evidenced by the absorption spectra of Figs. 1 and 2. The reduced matrix elements of Table I indicate that, for the $^4A_2\rightarrow{}^4T_2$ transition, the oscillator strength of the π-polarized light induced by the t_{2u} distortion is expected to be four times greater than that of the σ polarization; in agreement, the data in Figs. 1 and 2 show that the $^4A_2\rightarrow{}^4T_2$ band is stronger in the π spectrum. This effect is especially evident for the low-temperature spectrum, where the dynamically induced intensity is minimized. Similarly, the t_{2u} odd-parity distortion is calculated to only contribute intensity to the $^4A_2\rightarrow{}^4T_1a$ transition for the σ spectrum. The absorption spectra are also in agreement with this determination.

Also listed in Table I is the calculated transition strength of the $^4T_2\rightarrow{}^4T_1a$ excited-state absorption. While the ESA spectra will be discussed in much greater detail in Sec. IV, we remark at this time that one of the two Jahn-Teller split components of this transition (band 2 in Table I), does not receive any contribution to its intensity from the static t_{2u} field because the $\langle e\|a_2\|e\rangle$ reduced matrix element identically vanishes for d orbitals. (This is the case since the a_2 operator can only be described by spherical harmonics of rank 6 or higher,[14] while the $3d$ orbitals are linear combinations of rank-2 spherical harmonics.)

IV. EXCITED-STATE ABSORPTION SPECTRA

The results of the ESA measurements are shown in Figs. 5 and 6. The difference spectrum in Fig. 5 clearly shows the bleaching of the $^4A_2\rightarrow{}^4T_1a$ ground-state absorption (GSA) band centered near 23 500 cm^{-1} as a negative feature, as described by Eq. (2). The positive feature at 20 500 cm^{-1} corresponds to the $^4T_2\rightarrow{}^4T_1b$ ESA. Note that the difference spectrum has been absolutely calibrated by assigning the same cross section to the negative feature as that of the GSA band.

Additional support for the assignment of this ESA band in Fig. 5 to the $^4T_2\rightarrow{}^4T_1b$ transition comes from its predicted position and width. From the Tanabe-Sugano diagram in Fig. 3, the ESA transition energy in the absence of lattice relaxation is predicted to be 20 000 cm^{-1}, which agrees well with its measured value of 20 500 cm^{-1}, as shown in Fig. 5. Furthermore, since it involves a t_2^2e to t_2e^2 interconfigurational transition, this ESA band is expected, and is observed to be broad. The good agreement with predictions validates the assignment of this ESA band and the use of simple crystal field concepts in understanding the nature of this ESA transition.

The ir ESA spectra at 107 and 295 K are shown in Fig. 6. The spectra end at 10 000 cm^{-1} because the strong sample emission at higher energies overwhelms the weaker probe beam. This ESA band corresponds to the $^4T_2\rightarrow{}^4T_1a$ transition. The absolute cross section of the infrared ESA spectrum at 295 K was established by comparing its magnitude to the bleaching signal of the $^4A_2\rightarrow{}^4T_1a$ ground-state absorption peak. This calibration was not performed for the ESA spectrum at 107 K.

The Tanabe-Sugano diagram in Fig. 3 predicts the position of this ESA band to be 7600 cm^{-1}. This substantially disagrees with the measured ESA spectrum in Fig. 6, which clearly peaks at greater than 10 000 cm^{-1}. This transition is also expected to be narrow since both the

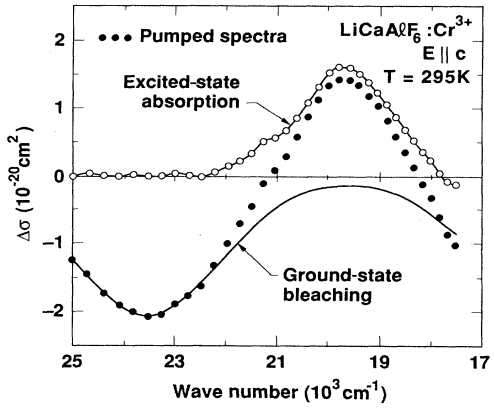

FIG. 5. Excited-state absorption and ground-state bleaching of $LiCaAlF_6:Cr^{3+}$ with E||c at 295 K. The $^4T_2 \rightarrow {}^4T_1 b$ excited-state transition is the positive feature while the negative signal arises from the bleaching of the $^4A_2 \rightarrow {}^4T_2$ ground-state absorption. Note that the ground-state absorption (solid line) was added to the experimental difference spectrum (solid circles) to derive the pure excited-state absorption spectrum (open circles).

$^4T_2$ and $^4T_1 a$ states are derived from the same $t_2^2 e$ configuration. This is again in striking contrast to the broad band observed in Fig. 6. These discrepancies between the predictions and the measured ir ESA have also been observed in other similar systems. In particular, Caird *et al.*[3] have found a similar ir ESA band for $Na_3Ga_2Li_3F_{12}:Cr^{3+}$ centered at 11 800 cm^{-1} with a full width at half maximum (FWHM) of 4000 cm^{-1}, and Payne *et al.*[2] observed a broad, blue-shifted ESA band in the infrared for the d^3 system of V^{2+} in various fluoride hosts. Andrews *et al.* also observed the broad infrared ESA band for the $Gd_3Sc_2Ga_3O_{12}:Cr^{3+}$ system.[1]

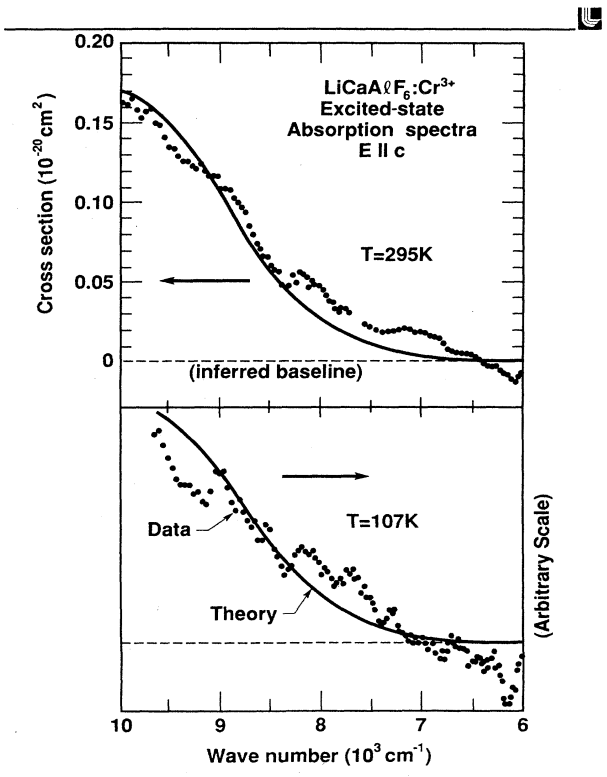

FIG. 6. Infrared excited-state absorption spectra of $LiCaAlF_6:Cr^{3+}$ at room temperature and 107 K. The spectra have been fit to Eqs. (11b) and (12) using the Jahn-Teller energy of $E_{JT} = 600\ cm^{-1}$.

Payne, Chase, and Wilke show that these discrepancies are manifestations of the Jahn-Teller effect in the $^4T_2$ and $^4T_1 a$ states arising from coupling to an e_g pseudolocal vibrational mode. We will show that a similar mechanism is relevant to this system. The details of this mechanism have been previously presented in a study of the ESA of V^{2+} in fluoride hosts.[2] We present a qualitative discussion of that theory here.

The effects on the $^4T_2 \rightarrow {}^4T_1 a$ ESA spectra of coupling to NTS vibrations are larger or comparable than the coupling to totally symmetric (TS) vibrations. This argument is supported by evidence obtained in the earlier work of Fairbank *et al.*,[15] in which various ESA transitions originating from the ^2E state of Cr^{3+} were studied. It was observed that if the terminal level was an orbital singlet, the ESA was narrow, consisting predominantly of zero-phonon character. This was true even when a configurational change was involved. However, if the terminal state was orbitally degenerate, only broad features were observed. For transitions involving the same change of electron configuration, the TS vibration is expected to affect all of these states about equally. However, to first order, the NTS vibration affects only the orbitally degenerate states. Thus, it was concluded that the dominant mechanism for the broadening of the ESA is coupling to NTS vibrations.

Coupling of a degenerate NTS vibration to an orbitally degenerate state results in a Jahn-Teller interaction. In perfect cubic symmetry, the pertinent Jahn-Teller active NTS vibrations are of e_g and t_{2g} symmetry. The e_g vibrations, which involve radial displacements, are expected to couple more strongly than the t_{2g} vibrations, which involve tangential displacements. Compelling evidence implicating the e_g vibration as the pertinent Jahn-Teller active mode in this system comes from the observation of a 452-cm^{-1} e_g vibration in the low-temperature emission spectrum.[16] Thus it is reasonable to consider the Jahn-Teller interaction of an e_g vibration with the two triply degenerate states, $^4T_2$ and $^4T_1 a$, involved in the ir ESA of Cr^{3+} in LiCAF. When the static local field departs from cubic symmetry, the problem becomes very complex. Hence, we will consider the case of perfect cubic symmetry for ease of discussion.

The case of a triply degenerate electronic state coupled to an e_g vibration has been previously described by Sturge and other workers.[17–19] In the absence of the spin-orbit interaction, the e_g vibration does not mix the orbital components of the $^4T_2$ or $^4T_1 a$ states, and we have vibrational potential energy surfaces consisting of three separate ("disjointed") paraboloids in the two-dimensional space of the Q_θ and Q_ϵ coordinates of the e_g vibration. For a transition involving a $^4T_2$ to a $^4T_1$ state,

it has been shown that the reduced matrix element of the first-order Jahn-Teller interaction is of opposite signs for the $^4T_2$ and $^4T_1$ states.[2] In other words, the $^4T_2$ and the $^4T_1$ states have their vibrational potential minima at opposite signs of the e_g vibration. It is this property that causes the blue shift and broadening of the ir ESA band to be so large.

To illustrate this, a cross section of the potential surfaces along the Q_θ axis is shown in Fig. 7. The arrows indicate the two possible Franck-Condon transitions for a system in the relaxed state of the ξ orbital of the $^4T_2$ state to the three sublevels of the ^4T_1a state. The energies of these two transitions are calculated to be[2]

$$E_1=\Delta E+E_{JT}\ , \tag{11a}$$

$$E_2=\Delta E+4E_{JT}\ , \tag{11b}$$

where ΔE is the separation of the $^4T_2$ and ^4T_1a states in the absence of the Jahn-Teller interaction and E_{JT} is the Jahn-Teller stabilization energy. Examination of the ESA data in Fig. 6 would seem to indicate the presence of only one transition. The transition labeled 2 is surmised to have a larger transition strength than 1, though their exact strengths are difficult to determine.[2] The FWHM of transition 2 is calculated to be[10]

$$\Delta_2=(32\ln 2)^{1/2}(E_{JT}\hbar\omega)^{1/2}\ , \tag{12}$$

for kT much less than $\hbar\omega/2$, where $\hbar\omega$ is the effective energy of the e_g vibration.

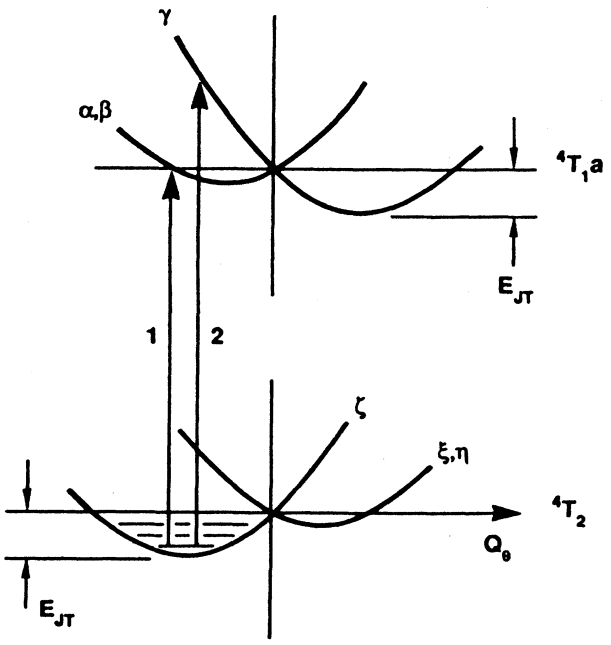

FIG. 7. Cross section of the adiabatic potential energy surfaces of the $^4T_2$ and ^4T_1a states along $Q_\epsilon=0$ in the e_g coordinate subspace. The labels ξ, n, ζ, α, β, and γ refer to the orbital components of the $^4T_2$ and ^4T_1a states transforming as yz, zx, xy, x, y, and z, respectively. The excited-state absorption transitions of Eqs. (11) are labeled 1 and 2.

The ESA data in Fig. 6 were fit with a Gaussian line shape using Eqs. (11b) and (12) for the peak position and width. Using a $\hbar\omega$ of 452 cm^{-1} in connection with the e_g vibration observed in low-temperature emission[16] and 7600 cm^{-1} for ΔE as indicated previously, this leaves E_{JT} as the only adjustable parameter for the fit. The result is shown as the solid line in Fig. 6. The fit is reasonable and gives $E_{JT}=600$ cm^{-1}. The ESA peak is predicted to be at 10 030 cm^{-1} and to have a FWHM of 2450 cm^{-1}. It is important to note that we have ignored any contributions to the broadening of the ESA band from displacements of other symmetries, such as a_{1g} and t_{2g}. This value of E_{JT} must therefore be regarded as an upper limit to the energy offset attributable to e_g distortions alone.

We note from Fig. 6 that the peak ESA cross section is 0.17×10^{-20} cm^2. On the other hand, the peak emission cross section was reported to be 1.3×10^{-20} cm^2 in Ref. 5. If the ESA cross-section value is extrapolated to the peak of the emission band at 13 200 cm^{-1}, the reduction of the stimulated emission cross section due to the influence of the ESA band is found to be negligible [see Eq. (1)]. The low ESA cross section is in agreement with the calculation presented in Sec. III B and Table I, where it was shown that the t_{2u} static distortion at the Al^{3+} site gives rise to the increased oscillator strength for the π-polarized $^4A_2\rightarrow{}^4T_2$ transition, while it does not add strength to band 2 of the $^4T_2\rightarrow{}^4T_1a$ ESA feature. Specifically, from Table I we see that band 2 is due to an $e_g\rightarrow e_g$ electron transition and is expected to have an intensity described by the reduced matrix element $|\langle e\|a_2\|e\rangle|^2/3$. This integral is identically zero for d orbitals for the reasons noted in Sec. III. This accounts for the low cross section of this ESA band, since the $^4T_2\rightarrow{}^4T_1a$ transition can, therefore, only be dynamically induced via odd-parity vibrations, while the $^4T_2\rightarrow{}^4A_2$ emission band is stronger since it is induced both dynamically and by the t_{2u} static field.

The question remains as to why band 1 of the $^4T_2\rightarrow{}^4T_1a$ transition is not observed. The answer is not completely certain, but, from Table I we see that this transition is a $t_{2g}\rightarrow t_{2g}$ type d-d transition, which can be distinguished from both the emission ($e_g\rightarrow t_{2g}$) and band 2 of the infrared ESA ($e_g\rightarrow e_g$). Thus, it is possible that the t_{2g} orbitals, in general, interact weakly with the fluorines and do not produce strong transition rates.

V. CONCLUSIONS

The ESA spectrum of the $^4T_2\rightarrow{}^4T_1a$ transition in LiCAF:Cr^{3+} is broadened and shifted to shorter wavelengths compared with predictions based on the usual assumptions of crystal-field theory. This behavior is caused by excited-state relaxation of the neighboring ions due to the coupling of the orbital triplet states to non-totally-symmetric distortions. Although the characteristics of this ESA band in LiCAF are similar to those observed for Cr^{3+} and V^{2+} in several other crystalline hosts, the magnitudes of the blue shift and the width of the band are

smaller in LiCAF:Cr^{3+} than, say, in $Na_3Ga_2Li_3F_{12}$:Cr^{3+} (hereafter GFG:Cr^{3+}), which results in a smaller overlap of the ESA band and the emission band. This is in agreement with predictions made by Caird *et al.*,[3] who argued that the stiffer local force constants resulting from a smaller substitutional site for the Cr^{3+} would have the effect of minimizing the excited-state relaxation.

The aspect of the infrared ESA band that is of greatest practical interest and impact is its very low absorption cross section in comparison with the ${}^4T_2 \rightarrow {}^4A_2$ emission cross section. This is caused by the particular symmetry of the odd-parity distortion at the Al^{3+} site; this distortion enhances the π-polarized emission (and absorption) cross sections, but it does not contribute at all to the ${}^4T_2 \rightarrow {}^4T_1 a$ ESA cross section. The combination of this lower ESA cross section and the decreased overlap of the emission and ESA bands is responsible for the much higher intrinsic slope efficiency of the LiCAF:Cr^{3+} laser[5] compared with GFG:Cr^{3+} and several other tunable Cr^{3+} lasers.[3]

ACKNOWLEDGMENTS

We wish to thank H. Newkirk for providing the Cr^{3+}:$LiCaAlF_6$ crystal, G. Wilke for acquiring all of the spectra reported in this paper, and G. Ullery for maintaining the flashlamp-pumped dye laser in the course of this work. Helpful discussions from Dr. William F. Krupke are gratefully acknowledged. This work was performed under the auspices of the Division of the Materials Sciences of the Office of Basic Energy Sciences, U.S. Department of Energy, and the Lawrence Livermore National Laboratory under Contract No. W-7405-ENG-48.

[1]L. J. Andrews, S. M. Hitelman, M. Kokta, and D. Gabbe, J. Chem. Phys. **84**, 5229 (1986).

[2]S. A. Payne, L. L. Chase, and G. D. Wilke, Phys. Rev. B **37**, 998 (1988).

[3]J. A. Caird, S. A. Payne, P. R. Staver, A. J. Ramponi, L. L. Chase, and W. F. Krupke, IEEE J. Quantum Electron. **24**, 1077 (1988).

[4]R. Moncorge and T. Benyattou, Phys. Rev. B **37**, 9177 (1988).

[5]S. A. Payne, L. L. Chase, H. W. Newkirk, L. K. Smith, and W. F. Krupke, J. Quantum. Electron. **24**, 2243 (1988).

[6]S. A. Payne, L. L. Chase, W. F. Krupke, and L. A. Boatner, J. Chem. Phys. **88**, 6751 (1988).

[7]Y. Tanabe and S. Sugano, J. Phys. Soc. Jpn. **9**, 766 (1954); D. L. Wood, J. Ferguson, K. Knox, and J. F. Dillon, J. Chem. Phys. **39**, 890 (1963).

[8]S. Sugano, Y. Tanabe, and H. Kamimura, *Multiplets of Transition-Metal Ions in Crystals* (Academic, New York, 1970).

[9]C. J. Ballhausen, *Introduction to the Ligand Field Theory* (McGraw-Hill, New York, 1962).

[10]A. M. Stoneham, *Theory of Defects in Solids* (Oxford University, Oxford, 1975).

[11]V. W. Viebahn, Z. Anorg. Allg. Chem. **386**, 335 (1971).

[12]J. I. Steinfeld, *Molecules and Radiation: An Introduction to Modern Molecular Spectroscopy* (MIT, Cambridge, 1974).

[13]The existence of the t_{2u} distortion was first recognized as a component of the Cr^{3+} site in ruby; M. Shinada, S. Sugano, and T. Kushida, J. Phys. Soc. Jpn. **21**, 1342 (1966).

[14]J. S. Griffith, *The Theory of Transition-Metal Ions* (Cambridge University Press, London, 1971).

[15]W. M. Fairbank, Jr., G. K. Klauminzer, and A. L. Schawlow, Phys. Rev. B **11**, 60 (1975).

[16]The low-temperature emission spectrum reveals the e_g mode frequency to be at 452 cm^{-1}. This corresponds well with the e_g frequency observed for Cr^{3+}-doped elpasolite hosts. See, e.g., J. Ferguson, H. J. Guggenheim, and D. L. Wood, J. Chem. Phys. **54**, 504 (1971); P. Greenough and A. G. Paulusz, *ibid.* **70**, 1967 (1979).

[17]M. D. Sturge, in *Solid State Physics,* edited by F. Seitz, D. Turnbull, and H. Ehrenreich (Academic, New York, 1967), Vol. 20.

[18]G. A. Slack, F. S. Ham, and R. M. Chrenko, Phys. Rev. **152**, 376 (1966).

[19]M. D. Sturge and H. J. Guggenheim, Phys. Rev. B **4**, 2092 (1971).